Nonlocal elastic metasurfaces: Enabling broadband wave control via intentional nonlocality

Hongfei Zhu[a,1], Sansit Patnaik[a], Timothy F. Walsh[b], Bradley H. Jared[c], and Fabio Semperlotti[a,1]

[a]Ray W. Herrick Laboratories, School of Mechanical Engineering, Purdue University, West Lafayette, IN 47907; [b]Simulation Modeling Sciences, Sandia National Laboratories, Albuquerque, NM 87185; and [c]Material, Physical and Chemical Sciences Center, Sandia National Laboratories, Albuquerque, NM 87185

Edited by J. B. Pendry, Imperial College London, London, United Kingdom, and approved September 4, 2020 (received for review March 17, 2020)

While elastic metasurfaces offer a remarkable and very effective approach to the subwavelength control of stress waves, their use in practical applications is severely hindered by intrinsically narrow band performance. In applications to electromagnetic and photonic metamaterials, some success in extending the operating dynamic range was obtained by using nonlocality. However, while electronic properties in natural materials can show significant nonlocal effects, even at the macroscales, in mechanics, nonlocality is a higher-order effect that becomes appreciable only at the microscales. This study introduces the concept of intentional nonlocality as a fundamental mechanism to design passive elastic metasurfaces capable of an exceptionally broadband operating range. The nonlocal behavior is achieved by exploiting nonlocal forces, conceptually akin to long-range interactions in nonlocal material microstructures, between subsets of resonant unit cells forming the metasurface. These long-range forces are obtained via carefully crafted flexible elements, whose specific geometry and local dynamics are designed to create remarkably complex transfer functions between multiple units. The resulting nonlocal coupling forces enable achieving phase-gradient profiles that are functions of the wavenumber of the incident wave. The identification of relevant design parameters and the assessment of their impact on performance are explored via a combination of semianalytical and numerical models. The nonlocal metasurface concept is tested, both numerically and experimentally, by embedding a total-internal-reflection design in a thin-plate waveguide. Results confirm the feasibility of the intentionally nonlocal design concept and its ability to achieve a fully passive and broadband wave control.

elastic metasurface | intentional nonlocality | total-internal-reflection | wave control | wave filtering

The concept of metasurface was originally pioneered in optics (1–8) and, shortly afterward, extended to acoustics (9–20). Metasurfaces quickly gained popularity thanks to their ability to achieve wave-front control via deep-subwavelength artificial interfaces. This characteristic stands in stark contrast with traditional metamaterials whose ability to control incoming wave fronts is limited by the strict dependence between the size and number of unit cells and the wavelength of the incoming wave. The most direct consequence of this physical constraint is the existence of a minimum dimension of a metamaterial slab (typically on the order of several wavelengths) that is necessary to control incoming waves. On the contrary, metasurfaces are very thin layers (typically a fraction of the dominant wavelength) that allow an abrupt control of the wave fronts, therefore offering a powerful alternative to circumvent a key practical limitation of metamaterials.

The response of a metasurface subject to an incoming wave is described by the Generalized Snell's Law (GSL) (1, 21), which allows predicting directions of anomalous reflection and refraction across an interface characterized by a spatial phase gradient. It is indeed this capability to encode the most diverse phase-gradient profiles within the metasurface that allows achieving unconventional effects, including, but not limited to, wave-front shaping (2, 8), surface-modes generation (7), and ultra-thin lenses (5, 6).

More recently, the concept of metasurface was also extended to elastodynamics (22–29) in an effort to achieve abrupt control of elastic waves in solid media. Initially, Zhu and Semperlotti (22) explored the behavior of an elastic metasurface in transmission mode and investigated the possibility of controlling the direction and the shape of a refracted wave front generated by an incoming planar wave. Later, the study was extended to show that metasurfaces could act as subwavelength barriers, therefore completely preventing the transmission of elastic waves across the interface (30, 31). Despite the great success in the application of metasurfaces to wave-front control and shaping, their intrinsic narrow-band performance has greatly limited their use in real-world applications. The limited operating frequency range is a direct consequence of the underlying design based on locally resonant unit cells. In passive metasurfaces, local resonances are used to achieve abrupt phase changes as propagating waves cross the interface. As the frequency of the incoming wave is detuned with respect to the operating frequency of the individual unit cells, the metasurface quickly loses its efficiency and ability to control the wave.

In order to address this important shortcoming of passive metasurfaces, researchers have explored the possibility to use active designs, involving piezoactuators and control logic, to extend the operating range. Chen et al. (32) introduced a programmable active elastic metasurface with sensing and actuating units that achieved wave-control functionalities over a

Significance

The practical application of passive elastic metasurfaces is severely hindered by its intrinsic narrow-band performance due to the underlying locally resonant nature. In this study, we present the concept of "intentional nonlocality" as the fundamental mechanism to design broadband elastic metasurfaces for the control of stress waves in solid media. The nonlocal design breaks the strict dependence on the local resonance of the unit cells and allows crafting an elaborate frequency-wavenumber-dependent response that guarantees remarkable broadband performance. This approach eliminates the most significant barrier to the development of elastic metasurface-based devices and paves the way to a wide range of practical applications.

Author contributions: H.Z. and F.S. designed research; H.Z. performed research; S.P., T.F.W., B.H.J., and F.S. contributed new reagents/analytic tools; H.Z., S.P., and F.S. analyzed data; and H.Z., S.P., T.F.W., B.H.J., and F.S. wrote the paper.

The authors declare no competing interest.

This article is a PNAS Direct Submission.

[1]To whom correspondence may be addressed. Email: zhu307@purdue.edu or fsemperl@purdue.edu.

This article contains supporting information online at https://www.pnas.org/lookup/suppl/doi:10.1073/pnas.2004753117/-/DCSupplemental.

First published October 5, 2020.

broadband range of harmonic signals. Despite the good success of the active approach, the overall increased complexity and the significant barriers in scaling the design to either larger structures or high-intensity waves make this approach not always viable. It follows that the ability to synthesize fully passive broadband designs still represents a major research endeavor and holds the potential to revolutionize elastic metasurface-based devices. As an example, the ability to shield sensitive electronic systems or infrastructures from incoming high-intensity waves (e.g., seismic or blast waves) would greatly benefit from broadband passive metasurfaces that could successfully divert the mechanical energy simply relying on thin ultra-subwavelength layers.

To address this major challenge, we introduce the concept of *intentional nonlocality*. The study and modeling of nonlocal system properties have been a long-standing challenge in many areas of engineering and physics. While the general concept of nonlocality holds a practically universal meaning strictly connected to the idea of action at a distance, technical nuances can arise, depending on the specific area of application. In classical mechanics of solids, the concept of nonlocality implies that the local response of the medium at a target location (typically expressed in terms of a stress field) does not only depend on the state of the medium (typically expressed in terms of a strain field) at that same location, but also from the state of other distant locations. The ensemble of these distant points, whose state affects the response at the target location, forms a surface (in two dimension) or a volume (in three dimension) known as the area, or volume, of influence. In elastodynamics, the concept of nonlocality results in a dependence of the stress (or, equivalently, the strain) field on the wavenumber (33–36). Note that, at the macroscale, the typical nonlocal character of many natural materials is very subtle, and, in most applications, it is considered as a higher-order effect.

The concept of nonlocality has also found applications in electromagnetisms and photonics; examples in the area of engineered materials include electromagnetic metasurfaces (37, 38), metagratings (39–41), and metamaterials (42–44). More recently, this concept was also extended to acoustic metamaterials (45–47) and metasurfaces (48). Despite these previous applications in other metamaterial systems, the concept of nonlocality in elastic metamaterials was not explored and implemented. In addition, none of the above systems explored an intentional use of nonlocality with the goal of achieving selected dynamic properties. The main reason why this area lags behind is to be found in the complexities related to accessing and exploiting nonlocality in the frame of elasticity. While electromagnetic and photonic applications can directly access materials that naturally exhibit a significant level of nonlocality (49–51), in mechanics, nonlocality is a higher-order effect that is typically appreciable only at the micro (or smaller) scales. To date, no attempts have been made to develop nonlocal elastic metasurfaces.

In this study, we propose the concept of intentional nonlocality that is introduced into the design of an elastic metasurface in order to extend its operating range by leveraging wavenumber-dependent mechanical properties. More specifically, starting from a classical locally resonant elastic metasurface design (22), we exploit the concept of *action-at-a-distance* by coupling selected unit cells via carefully designed connecting elements. These elements are conceived explicitly to create wavenumber-dependent coupling forces that mimic, at the macroscale, the nonlocal effect typical of nonlocal forces in elastic-continuum microstructures.

In this study, the concept of intentional nonlocality will be illustrated by applying it to a total-internal-reflection type of metasurface (TIR-MS) (30, 31), which was chosen as a basic benchmark system. Note that, despite this choice, the proposed concept is extremely general and applicable to any type of metasurface. *SI Appendix* presents a simple example of application to a transparent metasurface (*SI Appendix*, section 2G). A specific semianalytical transfer-matrix model was developed to study the effect of the nonlocality on the dynamic behavior of the metasurface and to facilitate the synthesis of practical physical designs for numerical and experimental testing. Then, the nonlocal TIR-MS (NL-TIR-MS) concept was embedded in a thin-plate waveguide, and its performance was assessed via a combination of numerical and experimental tests.

Methods and Materials

Fundamentals of Local Elastic Metasurface Design. In order to facilitate the understanding of the nonlocal design, this section provides a brief overview of the basic design principles of a classical passive elastic metasurface (22), which, in the following, will be referred to as the *local* design. In the classical problem of wave transmission across an interface between dissimilar materials, the angle of refraction is entirely determined by the impedance mismatch between the two materials, and it is carefully described by the Snell's law. For a given wavelength, the angle of refraction is fixed once the two materials are chosen. However, when in the presence of a metasurface that encodes a prescribed spatial phase gradient (along the metasurface direction), the refracted angle is no longer controlled only by the impedance mismatch between materials, but also by the phase gradient itself. In fact, metasurfaces are typically employed to control the reflection and refraction of waves between half-spaces made of the same material (hence, without an intrinsic impedance mismatch due to the host medium).

When in the presence of an interface with a spatial gradient profile (Fig. 1*A*), the direction of the refracted wave front is obtained from the GSL (1):

$$\frac{\sin(\theta_t)}{\lambda_t} - \frac{\sin(\theta_i)}{\lambda_i} = \frac{1}{2\pi}\frac{\mathrm{d}\phi}{\mathrm{d}y}, \qquad [1]$$

where $\mathrm{d}\phi/\mathrm{d}y$ is the phase gradient, while θ_i and θ_t indicate the directions of the incident and refracted waves, respectively.

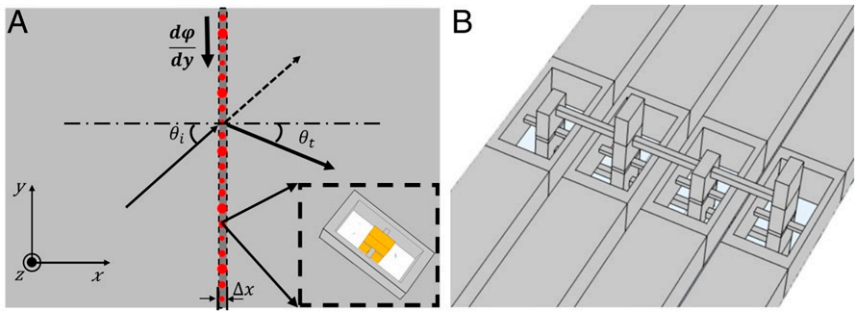

Fig. 1. (*A*) Schematic view of an elastic waveguide with an embedded local metasurface. Some of the fundamental parameters, such as the angle of incidence θ_i, the angle of anomalous refraction θ_t, and the phase gradient $\frac{\mathrm{d}\phi}{\mathrm{d}y}$, are shown. *A*, *Inset* also shows a schematic view of a typical locally resonant unit, from which the metasurface is assembled. (*B*) Schematic illustration introducing the concept of intentional nonlocality realized via flexible elements connecting different unit cells.

In passive elastic metasurfaces, the phase gradient is often realized by using a periodic array of locally resonant cells providing a linearly varying, step-like phase modulation covering the range [0, 2π]. Fig. 1*A* shows a conceptual view of a typical local elastic metasurface, as well as a zoomed-in view (black dashed box) of the locally resonant unit cell. The latter consists of a hollow frame with an internal resonator realized via a small mass attached to two slender beams connected to the frame. Previous studies (30, 31) showed that the dynamics of the resonator can be easily controlled in order to match specific phase profiles and design constraints, while limiting the fabrication complexity.

While, in the local design, the desired phase-gradient profiles can be efficiently achieved at a single target frequency, it is not possible to maintain the target phase gradient over a wide frequency range. This limitation is a direct consequence of the fundamental operating mechanism of the metasurface based on local resonances. A possible approach to overcome this limitation could include the design of multiresonant unit cells (e.g., using internal multi-degree-of-freedom resonators) within the basic local metasurface design. The increased number of design parameters would improve the ability to tune the phase-gradient profile versus frequency. Although conceptually possible, this approach would likely result in a very complex design of the unit cells, in a discrete type of control, and in an operating range still limited by the total number of local resonances available per unit cell (see more discussions in *SI Appendix*, section 1C).

Basic Concept and Mechanics of the Nonlocal Supercell. In the case of an elastic metasurface, a possible implementation of the nonlocal design is shown in Fig. 1*B*. The design relies on flexible beam-like links that connect the resonators of multiple distant units. This approach implements, at a macroscopic level, the basic concept of *action-at-a-distance* and results in the formation of a nonlocal supercell. The nonlocal supercell consists of a prescribed number of locally resonant units whose internal resonators are coupled to each other via specifically designed flexible links. Despite this physical implementation, we anticipate that the fundamental operating mechanism does not rely on the concept of a coupled resonator design. This topic is extensively discussed below and in *SI Appendix*. Given a basic nonlocal supercell design, the metasurface can be assembled by creating a periodic distribution of identical nonlocal supercells.

The remainder of this section addresses in detail both the source and role of nonlocality in our metasurface design. As will be evident in the following discussion, the nonlocality manifests itself in different (but all interrelated) ways. Therefore, we will discuss its role both from a physical and a mathematical perspective in order to provide a comprehensive account of the use of nonlocality to achieve target dynamic performance.

Origin and role of nonlocality. The proposed design is based on and implements, at a macroscopic level, the concept of action-at-a-distance. By using carefully designed mechanical links between pairs of units separated by a finite distance, our design represents the conceptual equivalent (in the form of a discrete macroscopic medium) of the long-range interactions typical of nonlocal materials. From a high-level perspective, a nonlocal material is defined as a medium in which the mechanical response at a given point (typically expressed in terms of stress) is affected by the state of all of the surrounding points (expressed in terms of strain) in a given area or volume, the so-called horizon of nonlocality. This definition is in contrast with that of local media, in which the stress at a point is only a function of the state of strain at that same point. While this definition is typically provided within a static context, it does apply identically to any type of response (e.g., to dynamic and stability analyses). However, when considering the dynamic response of a medium, the nonlocal action also manifests itself in additional ways. A classical example of the effect of nonlocal actions on the dynamic response of a medium is the dependence of the elastic material properties on the wavenumber. While this property is often indicated as the distinctive characteristic of dynamic nonlocal media, we stress that this is simply a different statement of the same concept of static nonlocality (that is, of the dependence of the response on the state of the medium represented, for example, by the spatial distribution of strain).

Although the intentional use of long-range connections makes the supercell nonlocal by design, we also corroborate our statement by mathematically showing that the effective elastic continuum representing the metasurface maps, indeed, to a nonlocal medium.

Consider a simplified one-dimensional (1D) discrete model, as illustrated in Fig. 2. The model is intended to simulate only the section of the nonlocal metasurface in order to illustrate the role and effect of long-range connections. The lattice model consists of N identical supercells with a lattice constant a. Each supercell counts three masses M that mimic the mass-in-mass units. Note that both the locally resonant nature of the unit and their different mass values are neglected in order to yield a more streamlined mathematical representation. These assumptions do not limit the overall goal of the model that is to show that long-range connections are the main elements responsible for the emergence of the nonlocal behavior and of the wavenumber-dependent elastic properties. In fact, the choice of neglecting local resonances strengthens even further the statement that the nonlocal properties are not due to resonance effects. The units are connected by springs which mimic both the local (k) and nonlocal (k') interactions, as illustrated in Fig. 2. The comparison in Fig. 2*B* shows the correspondence between the elements of the 1D model and the physical design. Note that the local connections are those occurring via the supporting plate, while the nonlocal connections are the links added between the masses (both between consecutive and distant masses).

In order to show that the equivalent continuum has wavenumber-dependent elastic properties due to the presence of the long-range connections, we first derive the dispersion relation for the discrete lattice system, and then we perform a continualization process combined with the classical Eringen integral approach to nonlocal elasticity (34, 36). While the complete mathematical details are reported in *SI Appendix*, section 1A, here,

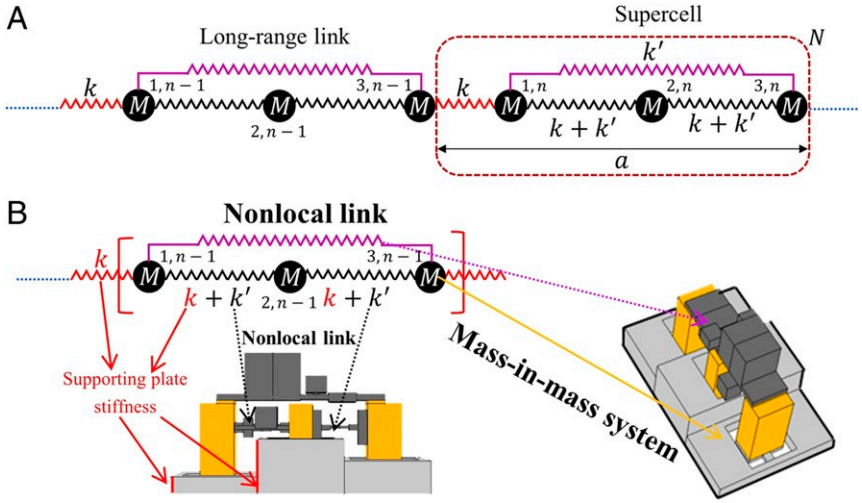

Fig. 2. (*A*) Schematic of the 1D discrete equivalent model of the metasurface and the corresponding supercell unit. The schematic illustrates the classical nearest-neighbor and next-nearest-neighbor interactions between the masses within the supercell. The red colored springs indicate purely local interactions (k), the magenta colored springs indicate purely nonlocal interactions (k'), and the black colored springs indicate a combination of local and nonlocal interactions ($k + k'$). *B* shows the correspondences between the simplified model and the physical design of the nonlocal supercell.

below, we report the resulting form of the effective elastic material properties describing the metasurface. These properties are provided in the form of Lamé constants for the equivalent nonlocal solid (34):

$$\overline{\lambda}'(\mathcal{K})+2\overline{\mu}'(\mathcal{K})=\left(\frac{\lambda+2\mu}{\sqrt{2\pi}}\right)\left[\frac{2(1+\phi)}{a^2\mathcal{K}^2}+\frac{[\overline{\psi}(\mathcal{K})]^{\frac{1}{3}}}{3a^2\mathcal{K}^2}+\left[\frac{3(1+\phi)^2-4\phi\sin^2(\mathcal{K}a/2)}{a^2\mathcal{K}^2}\right]\left[\overline{\psi}(\mathcal{K})\right]^{-\frac{1}{3}}-1\right], \quad [2]$$

where $\mathcal{K}$ denotes the wavenumber in the metasurface, $\phi=k'/k$ is a nondimensional ratio defining the strength of the nonlocal interactions, solid $\overline{\psi}(\mathcal{K})$ is a function of the wavenumber $\mathcal{K}$ and ϕ, and λ and μ are the Lamé constants of the corresponding local solid. The $\overline{\square}$ indicate Fourier-transformed quantities in space. Eq. **2** clearly shows the dependence of the effective elastic properties of the metasurface on the wavenumber. Note that, as the strength of the nonlocal contributions vanishes, then λ', $\mu'\to 0$, hence recovering the local case (see details in *SI Appendix*). *SI Appendix* provides additional considerations to help in interpreting and contrasting the role of the different simplified models used in this study.

Role of the nonlocal properties in achieving broadband behavior. The previous section confirmed that the introduction of the long-range connections induces a wavenumber dependence in the equivalent elastic properties of the metasurface. Interestingly, this unique dependence offers two complementary mechanisms to control the dynamic behavior of the metasurface.

Recall the duality that the dispersion relation of a medium establishes between wavenumber and frequency. The dispersion is typically expressed in the general form $\omega=\omega(|\vec{k}_i|)$, or, equivalently, $|\vec{k}_i|=|\vec{k}_i|(\omega)$, where ω is the circular frequency, and $\vec{k}_i$ is the wavevector. For the simple case of bulk local media (or even for simple structural elements like strings and rods), the medium is nondispersive, which results in a constant wave speed. However, if the bulk medium is nonlocal, it does acquire a frequency dependence via the wavenumber dependence of the elastic properties. Clearly, this dependence is maintained also for the more complex case of waveguides that are naturally dispersive, even in their local form. For nonlocal waveguides or dispersive media, the general-dispersion relation acquires the form $c=c(|\vec{k}_i|,\omega)$. In this latter case, the effect of the wavenumber dependence combines and superimposes with the frequency-dependent dispersion typical of waveguides; hence, its effect is less evident to isolate and recognize.

The above discussion suggests that nonlocality can be leveraged in two different, but complementary, ways—that is, by exploiting: 1) its direct (or explicit) effect on the wavenumber, and 2) its indirect (or implicit) effect on frequency (via the wavenumber). A detailed discussion of these dependencies is reported in *SI Appendix*, section 1B.

Difference between the proposed nonlocal design and a coupled resonator design. The proposed nonlocal design is not equivalent and does not operate as a coupled resonator system. While a more detailed discussion is reported in *SI Appendix*, section 1C, here, we highlight the most significant differences. Systems of coupled resonators have been used in the context of elastic metamaterials in order to achieve either vibration or bandgap control (52–54). However, these studies leveraged the coupling only as a mechanism to achieve multiple resonances and exploited the principle of vibration localization, which occurs in the scattering regime (as opposed to the homogenized regime, in which the nonlocal design operates). Our nonlocal design does not add any additional resonator, but leverages long-range, spatially dependent forces to create a complex frequency and wavenumber-dependent dynamics of the metasurface.

Results and Discussions

NL-TIR-MS. To illustrate the concept of nonlocality, we apply it to the design of a NL-TIR-MS (30) embedded in a plate waveguide. We recall that a local TIR-MS (30, 31) consists of a metasurface that is specifically designed to exhibit a phase-gradient profile meeting the requirement for total internal reflection. Under these conditions, incoming waves with any arbitrary angle of incidence (but in the neighborhood of the target operating frequency—i.e., the resonance frequency of the local unit cells) will not be able to cross the interface and will be reflected back. Note that the selection of the TIR-MS as a benchmark system to test the nonlocal concept does not limit the generality of the results. Similar performance can be envisioned also for transparent metasurfaces.

Basic design elements. In order to obtain complex phase-gradient profiles over an extended frequency range, the connecting elements must exhibit an elaborate local dynamics that can be obtained by using proper choices of the cross-sectional properties, materials, and local resonances. Within this general design framework, the synthesis of the links' final configuration requires the formulation and solution of an optimization problem. The objective of the optimization procedure is to select the links' physical parameters capable of producing the desired nonlocal forces that ultimately enable maintaining the target phase profile. Dedicated analysis tools are needed in order to simulate the response of these nonlocal systems—specifically, to understand the effect of the design parameters on the physical behavior of the supercell and to allow the synthesis of physically realizable designs. The overall modeling approach implements the following strategy. The nonlocal supercells are initially modeled by using simplified lumped parameter (e.g., mass-spring) systems that allows formulating the system dynamics via the transfer-matrix (TM) method. In the TM approach, the resonant unit is represented via a lumped parameter system, conceptually shown in Fig. 3*A*, which allows for capturing the relevant dynamics while requiring a reduced set of system parameters. This simplified approach is possible because the metasurface operates within a deep-subwavelength regime (i.e., the dominant wavelength is much larger than the characteristic unit-cell dimension). In addition, the long-range coupling forces between local unit cells can be simulated by means of mass-spring connections having frequency-dependent properties. Once the unit cells are coupled to form the *nonlocal* supercell, the links' parameters can be tuned to achieve a frequency-dependent phase profile. The details of the TM model, as well as some numerical results of a nonlocal supercell, are reported in *SI Appendix*, section 2.

Design of the NL-TIR supercell. In the following, we briefly illustrate the design procedure on the TIR nonlocal supercell. Both the metasurface and the host waveguide have thickness $h=6.35$ mm. The target operating bandwidth is set to $\Delta f=[4.2,5.7]$ kHz. Note that this selection of the operating range is somewhat arbitrary, and it was chosen exclusively for convenience of the experimental measurement. The nonlocal approach per se is not limited to a specific frequency range. The overall dimensions of the basic unit are $L(=20\ mm)\times W(=10\ mm)\times h(=6.35\ mm)$, as shown in Fig. 3*A*. Recall that, in order to ensure TIR conditions (30), the phase-shift gradient should always exceed the critical value $\mathrm{d}\phi/\mathrm{d}y=4\pi/\lambda$, and the transmission coefficients of each unit should have a comparable value. Assuming that the supercell contains n basic units to cover the 2π range, then it must be $\frac{2\pi}{nW}\geq 4\pi/\lambda$, which results in a condition on the number of units $n\leq\frac{\lambda}{2W}$. Over the selected frequency range, the wavelength λ approximately varies between $12.3\ W$ and $10.1\ W$; hence, a nonlocal supercell of $n=3$ units would fulfill the TIR criterion. Note that the three-unit supercell implementation represents a classical case of nearest-neighbor and next-nearest-neighbor interaction typical of many nonlocal systems. While more units could certainly be envisioned in order to achieve even a more general frequency response, this choice does not affect the generality of the proposed concept (see also *SI Appendix*, section 1D). Indeed, the choice of using a limited number of units simplifies the design and facilitates the explanation and the understanding of the role of different elements and their operating principle.

Assuming three basic units, the synthesis of the physical design (that is, the link that exhibits the desired effective dynamic properties predicted by the TM method) requires an optimization approach. To achieve a physical design, the procedure is

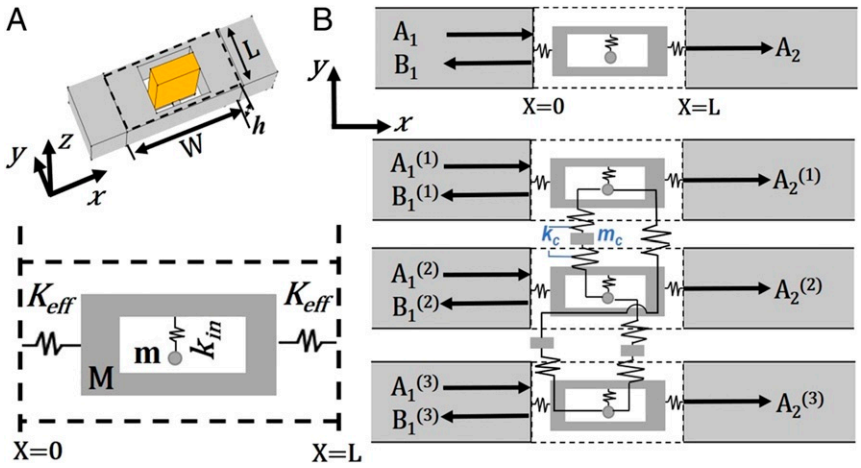

Fig. 3. Schematics illustrating the representation of the unit-cell model in discrete form. This representation is at the basis of the development of the TM model. (*A*) Schematic of a typical locally resonant unit cell (*Upper*) and its lumped-parameter counterpart represented by a mass-in-mass-spring model (*Lower*). (*B*, *Upper*) Schematic showing the integration of the lumped unit-cell model within an elastic waveguide, as well as the amplitude of the incident (A_1), reflected (B_1), and transmitted (A_2) waves. (*B*, *Lower*) Schematic showing the integration of local resonant units to form a nonlocal supercell. The connecting links are represented by lumped elements having stiffness k_c and mass m_c. The superscript in the amplitude coefficients represents the units number.

separated into three main steps: 1) select the fundamental unit cells; 2) identify the necessary profiles of nonlocal interaction force versus frequency; and 3) synthesize the physical design of the links capable of realizing the target nonlocal force profiles. These three steps are further elaborated in the following.

Step 1. The first step consists of selecting the physical design of the locally resonant unit cells. Note that, contrarily to the local design (22), which requires setting the fundamental resonance of the unit cells at the target frequency, in the nonlocal design, the individual unit cells do not need to be designed for a specific frequency. In fact, it is even preferable not to start with units operating at the same frequency because this would bias the dynamic behavior of the nonlocal metasurface in favor of a single frequency. The most direct effect of this bias would be the need for extreme values of the effective properties (e.g., either zero or negative mass and stiffness values) of the links in order to guarantee broadband performance. On the other side, an appropriate selection of the basic units can facilitate achieving a broadband design. In general, it was found to be a good design rule for the nonlocal metasurface to select units whose phase contribution (compared with the adjacent units) is close to $2\pi/n$ (where $n = 3$ in the present case) over the selected frequency range. This first step of the design can be performed by acting on the basic geometric parameters of the unit cells in order to tune their local resonances and, consequently, the phase profile. For the example presented in this study, the three selected units are shown in Fig. 4*A*. Details on the geometric design can be found in *SI Appendix*, section 3A. Their amplitude and phase responses were extracted by using the discrete TM model, and the results are summarized in Fig. 4 *B* and *C*. It can be seen that, although the phase profiles of the three units are slowly varying over the selected frequency range 0, $2\pi/3$, and $-2\pi/3$, the corresponding phase jumps between adjacent units (Fig. 4*B*) are always in the neighborhood of the target value.

Step 2. Once the fundamental resonant units forming the supercell are selected, the next step requires the identification of the nonlocal interaction forces needed to achieve the target performance of the TIR-MS over the selected operating range. Equivalently, the former objective can be stated by saying that the frequency-dependent effective properties (i.e., $m_c(\omega)$ and $k_c(\omega)$) that identify the dynamics of each connecting element must be determined, such that the phase jump between adjacent units is maintained at the constant value $2\pi/3$. Note that, although the amplitude of the response of each unit should also be maintained to comparable levels to each other (a condition

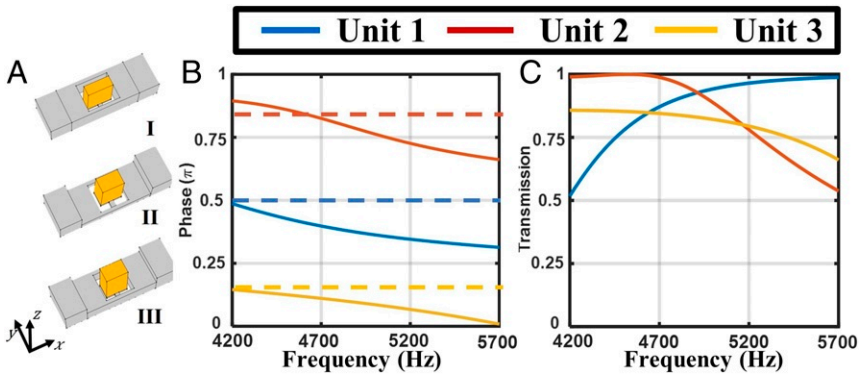

Fig. 4. (*A*) Schematics of the three selected locally resonant unit cells that will form the basis for the NL-TIR-MS. *B* and *C* show both the transmission phase and the transmission amplitude versus frequency for the three individual units.

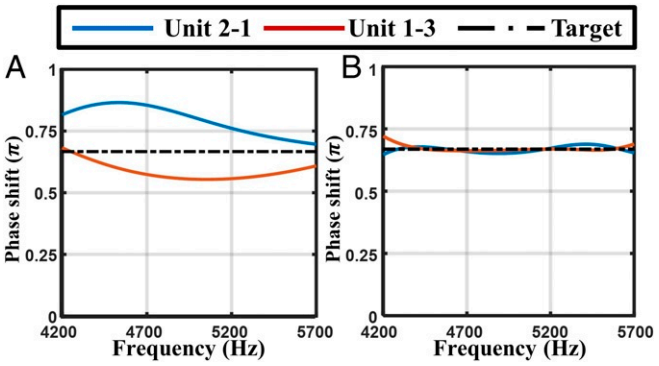

Fig. 5. (*A*) The phase shift of the local supercell without coupling elements. (*B*) The predicted phase shift from the lumped nonlocal supercell model after the application of the optimized coupling elements.

that guarantees the transmission coefficients of each unit to be equivalent), for the TIR-MS design, the ability to guarantee a constant phase gradient poses a more stringent requirement. In other terms, the ability to yield the desired phase gradient is more important than matching the response amplitude at the unit level. In a previous study on a local TIR-MS design (31), the authors illustrated this aspect in a more quantitative fashion.

The phase-shift response of the local and nonlocal three-unit supercell under normal incidence conditions is presented in Fig. 5 *A* and *B*, respectively. Results show that the nonlocal design is capable of producing a reasonably constant phase shift at the desired value $2\pi/3$. The corresponding effective properties characterizing the three coupling elements are shown in Fig. 6 *A*–*C*, respectively. For the sake of completeness, we further examined the dependence of the phase gradients on the wavenumber in the TIR design after obtaining these coupling elements. The phase-shift profile versus frequency, parameterized in terms of the angle of incidence, is presented in *SI Appendix*, Fig. S8. It is clear that different wavenumbers (i.e., angle of incidence) experience different phase shifts. For the TIR design, these deviations are limited because the goal is to maintain the target value $2\pi/3$. It is also noticeable that the deviation is more evident at higher frequencies, which also explains the deterioration of the performance.

A visual analysis of these wavenumber-dependent functions allows making an important consideration. The dynamic mass profile of coupling element 2 (Fig. 6*B*) shows a sharp variation around 5.4 kHz. While at this stage, we are dealing with synthetic coupling forces (i.e., effective forces not yet associated with a physical design of the link), this result suggests that, to be able to achieve such a sharp change in the dynamic properties of the link, a local resonance should be exploited. It is also worth noting that, this being the result of an inverse problem, the set of force profiles discussed above is only one of the many possible solutions.

Step 3. Once the necessary dynamic mass and stiffness profiles of the connecting elements are identified, the third and last step consists of converting these synthetic long-range transfer functions into physically realizable designs of the three coupling elements. To simplify the design process and avoid the need for topology optimization, we assume that the basic geometry of the connecting elements is fixed to be a thin rectangular beam having piece-wise constant thickness. While changes in thickness can help controlling the flexibility and the global dynamics of the link, it was already pointed out that sharp variations in the coupling forces requires local resonances. Hence, the beam connectors could also include attached resonators tuned at selected frequencies. Also in this case, in order to avoid the use of topology optimization, we assumed these resonators to be designed always in the form of cantilever dumbbells.

Based on the above assumptions, the topology of the links is entirely defined, so that the profiles of the effective properties (or, equivalently, of the nonlocal coupling forces) can be matched by performing a simple parameter optimization on the geometric design variables. This step was performed by using a commercial finite-element-based optimizer (COMSOL Multiphysics). The resulting physical configurations of the three coupling beams are shown in Fig. 7, and their dynamic responses are evaluated in Fig. 7 (dashed lines) and compared with the target profiles (solid lines). Overall, the dynamic properties of the three beams are in good agreement with the target profiles. We emphasize that the main goal of this study is to present and validate the concept of intentionally nonlocal metasurfaces, not to establish optimal designs and performance. Hence, these results should not be taken as indicative of best performance. Indeed, it is foreseeable that the use of a concurrent optimization approach might provide a better match of the nonlocal coupling terms and overall higher performance. The approach followed in this study was explicitly designed to illustrate the importance of intentional nonlocality and to characterize the role of the different design components, which would otherwise be lost if using only a purely numerical optimization approach.

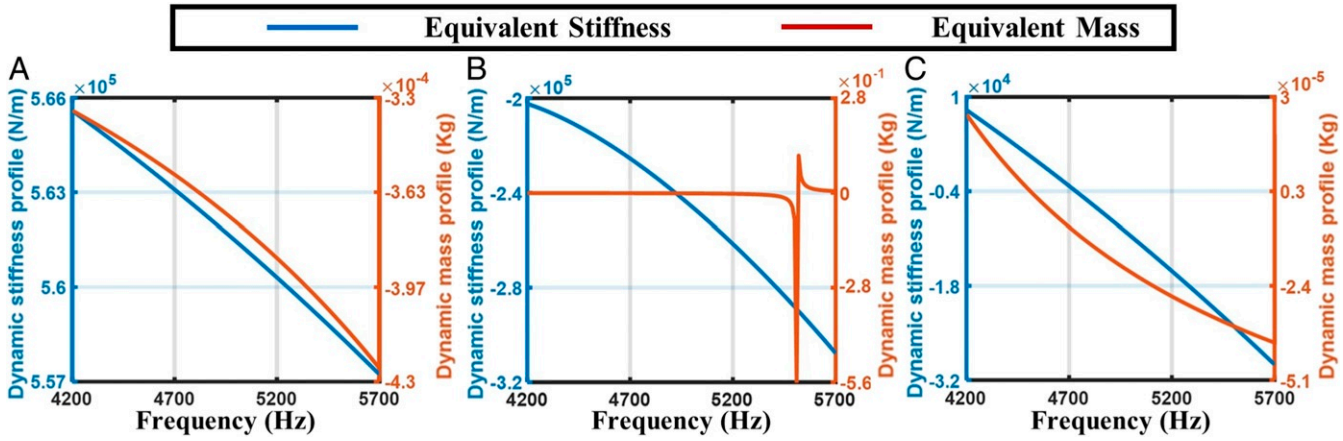

Fig. 6. The required dynamic stiffness and dynamic mass profiles necessary to achieve the broadband TIR effect. Results are presented for the three coupling beams: beam I (connecting unit 1 to 2) (*A*), beam II (connecting unit 2 to 3) (*B*), and beam III (connecting unit 1 to 3) (*C*).

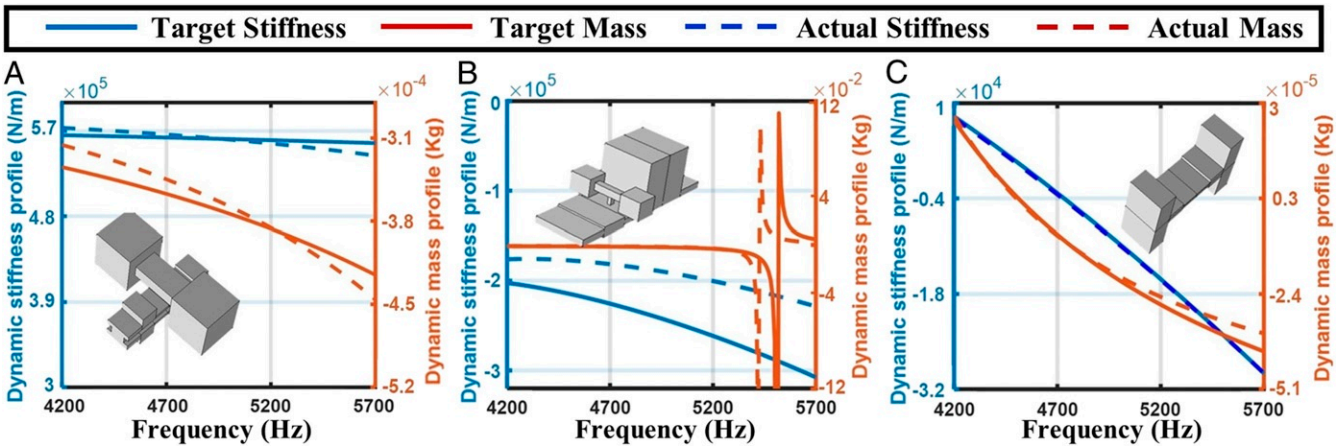

Fig. 7. Comparison of the dynamic stiffness and dynamic mass profiles provided by the synthetic (dashed lines) and the physical (solid lines) designs. *Insets* show the corresponding physical design of the beam connectors and local resonators: beam I (*A*), beam II (*B*), and beam III (*C*).

Numerical Results. The previous section presented the physical design of the connecting elements capable of achieving a broadband TIR effect. Based on this physical design, a complete three-dimensional (3D) model of the nonlocal metasurface (Fig. 8*A*) embedded in a flat plate was assembled. Note that the nonlocal metasurface was simply obtained by periodically repeating the basic nonlocal supercell (Fig. 8 *A*, *Inset I*) along the interface direction. The side view of the nonlocal supercell ($y-z$ plane) is also provided (Fig. 8 *A*, *Inset II*) in order to clarify the connection strategy between units. Further details on the connection scheme can be found in *SI Appendix*, section 3 B and C.

The waveguide with the embedded nonlocal metasurface was modeled via finite-element analysis using a commercial software (Comsol Multiphysics). The metasurface was excited by a point-load source located at a distance of 0.12 m from the plane of the metasurface (white star marker in Fig. 8*C*) and acting in the

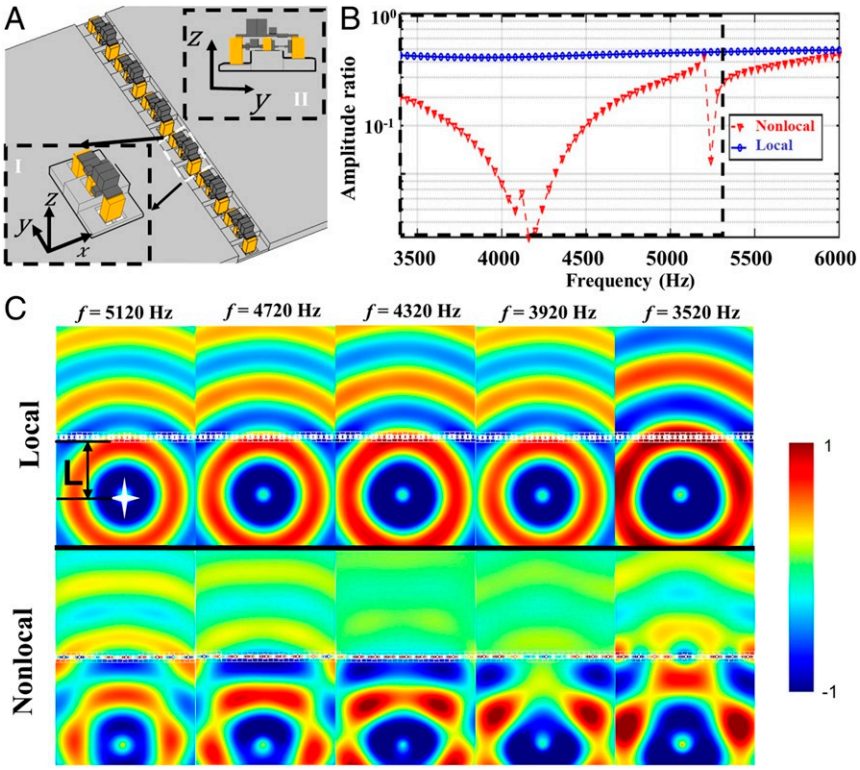

Fig. 8. Numerical simulations obtained from a full 3D model showing the performance of the NL-TIR metasurface. (*A*) Schematics showing the 3D model of the assembled NL-TIR-MS embedded in a thin waveguide. *A*, *Insets* show the isometric (*Inset I*) and the side (*Inset II*) view of the nonlocal connectors mounted on the resonating cores. Different components are marked by colors: basic unit cells, yellow; and connecting links, dark gray. (*B*) Spatially averaged amplitude ratio of the out-of-plane component of the velocity obtained from the response of the waveguide before and after the MS interface. Both local and nonlocal designs are compared. The wide dip observed in the nonlocal MS response (highlighted by the dashed black box) indicates the broadband wave-blocking effect. (*C*) Full-field simulations showing the out-of-plane particle displacement at five selected frequencies within the nonlocal MS operating range. The white star marker shows the location of the point-load source excitation.

out-of-plane $z-$direction, hence generating predominantly A_0 guided modes. Perfectly matched layers (PMLs) were applied at all of the boundaries to eliminate the effect of unwanted reflections. In order to assess the effect of the nonlocal metasurface on the propagating wave, the model of the equivalent local metasurface design was developed and used as a reference. This model consisted of the same set of resonant unit cells as those used in the NL-TIR-MS design, but without the nonlocal connections and the large masses (drawings provided in *SI Appendix*, Fig. S15).

Fig. 8*B* shows the comparison of the spatially averaged amplitude ratios calculated from the transverse particle displacement ($z-$direction) before and after the MS. Note that this specific ratio is only one of the different metrics that could be used to assess the behavior of the metasurface. This ratio provides a good quantitative estimate of the percentage of "mechanical energy" that propagates across the metasurface following a given incident wave. The spatial-averaging process helps in smoothing out possible local variations due to the scatterer, thus providing a more reliable indicator to track the behavior of the metasurface. Fig. 8*B* shows both the reference (local) MS and the NL-TIR-MS. The large reduction in the amplitude ratio of the NL-TIR-MS waveguide (marked by the dashed black box in Fig. 8*B*) compared with the reference waveguide is a clear indicator of the broad operating range of the proposed nonlocal design. Full-field numerical results are shown in Fig. 8*C* for five selected frequencies inside the operating bandwidth. The results are still presented in terms of out-of-plane particle displacement of the A_0 wave field. The direct comparison of these wave patterns shows that, although a small fraction of the incident wave front can still be transmitted through the metasurface, the nonlocal design is capable of producing a drastic reduction of the transmitted wave intensity over a broad frequency range.

In order to put these results in perspective, note that the numerically calculated bandwidth for the nonlocal design (approximately $\Delta f = [3.5, 5.1]$ kHz) corresponds to a 37.2% relative bandwidth with respect to its center frequency $f_0 = 4.3$ kHz. Compared to previous studies on local TIR-MS (30, 31), where available data showed approximately a 250-Hz bandwidth (only 4.54% of the center frequency $f_0 = 5.5$ kHz), the nonlocal design provides a range that is approximately eight times larger.

Experimental Validation. In order to validate the concept of intentional nonlocality as a viable approach to the synthesis of passive broadband metasurfaces and to confirm the performance of the NL-TIR-MS, we built an experimental test bed following the configuration that was numerically studied in Fig. 8*A*. The plate waveguide and the supporting frames of each resonant unit cell were made out of aluminum and fabricated via computer-numerical-control (CNC) machining. The nonlocal connecting links (including the three resonating masses) were made out of 316L stainless steel and fabricated via additive manufacturing techniques (i.e., metal printing). The links were later glued on the corresponding unit-cell slots. Further details on the fabrication process are discussed in *SI Appendix*, section 3D.

The test setup is shown in Fig. 9. Fig. 9*A* provides a front view of the setup consisting of a plate waveguide with the embedded nonlocal MS, while Fig. 9*B* shows a closeup view of the metasurface. In Fig. 9*C*, from top to bottom, the three panels show different views (Iso, Front, and Top) of the nonlocal links assembled on the three resonant masses. The plate waveguide was mounted in an aluminum frame, while a single Micro-Fiber-Composite (MFC) actuator was glued on the surface of the plate in order to apply the external excitation (red star marker in Fig. 9*A*). Viscoelastic tapes were applied all around the boundary of the plate so as to reduce back-scattering. The response

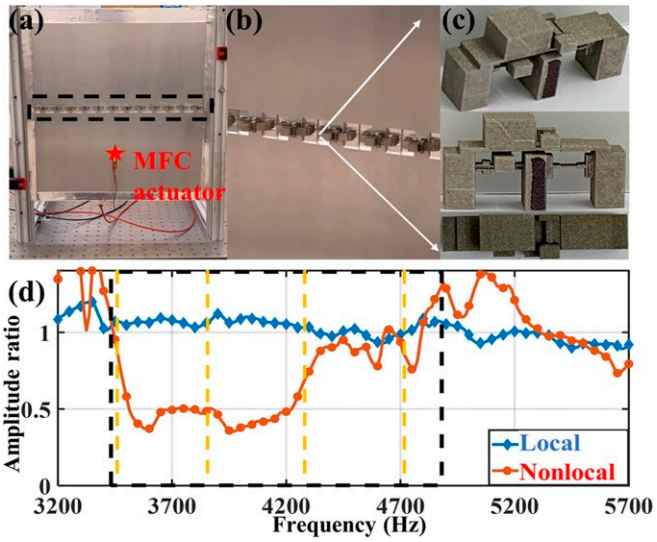

Fig. 9. Experimental setup consisting of a thin-plate waveguide with an embedded NL-TIR-MS. The waveguide was inserted into an aluminum frame providing a clamped boundary condition on two sides of the waveguide. The excitation was provided by an MFC patch glued on the surface (red star marker). (*A*) The front view of the experimental test bed. (*B*) Zoomed-in view of the NL-TIR-MS. (*C*) The 3D metal printed nonlocal beams mounted on the resonating masses. Three views are shown (Iso, Front, and Top), moving from *C, Top* to *C, Bottom* panel. The connectors are later glued in place on the corresponding unit cells realized in the supporting waveguide. (*D*) The spatially averaged amplitude ratio obtained from the measured out-of-plane velocity field before and after the MS. The comparison between the local and the nonlocal design clearly shows the broadband nature of the latter, which is highlighted by the large drop in the amplitude ratio (dashed black box).

of the plate was measured under white-noise excitation (bandwidth 3 to 6 kHz) by using a scanning laser Doppler vibrometer. Both the local (reference) and the nonlocal configurations were tested.

Fig. 9*D* presents the comparison of the spatially averaged amplitude ratios collected from the measured out-of-plane particle velocity in the regions before and after the MS. As already discussed for the numerical results, the large reduction in the amplitude ratio in the frequency band 3.55 to 4.55 kHz (black dashed box in Fig. 9*D*) identifies the region in which the nonlocal metasurface is effective and provides broadband wave-blocking effect. Note that, although the operating range is slightly smaller than the one predicted via numerical simulations, it still covers a range of 1 kHz—that is approximately a 24.69% relative bandwidth with respect to the center frequency $f_0 = 4.05$ kHz. Compared to the numerical results, we observed a reduction in the operating range and a global shift toward lower frequencies. These differences were due to structural modifications applied to the original design during the fabrication phase, to some variability in the properties of the 3D-printed connecting beams, to the coarseness of the printing process, and to inaccuracies during the manual assembly procedure of the nonlocal links (which were glued on location). Note that the shorter wavelengths obtained at higher frequency became progressively more sensitive to small changes in geometric features and to fabrication errors. We also note that the averaged amplitude ratio observed in the experimental data appears to be significantly higher than the numerical predictions. This difference was due to the boundary conditions applied in the experimental setup, as opposed to those used in the numerical model. The numerical model employed PMLs that absorbed entirely any incoming wave, hence simulating an infinite domain. In the experimental setup, the size of the domain was finite and, while the boundaries were treated

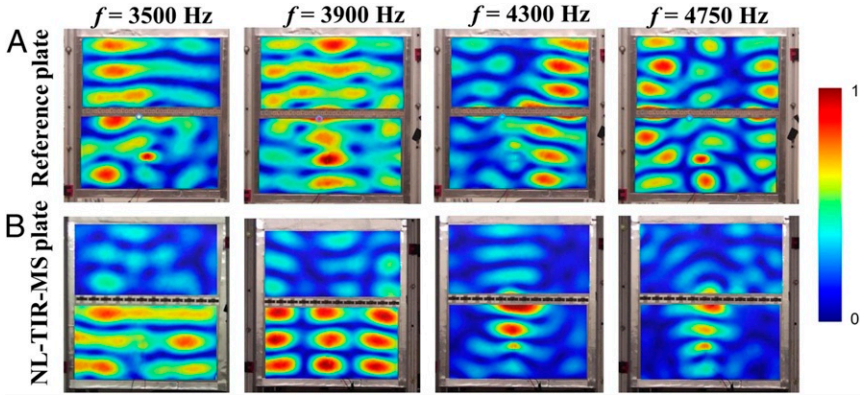

Fig. 10. Full-field experimental data showing the performance of the NL-TIR-MS in comparison to the local design. The images show the out-of-plane particle-velocity field at four selected frequencies within the operating bandwidth of the nonlocal MS. (*A*) The out-of-plane particle-velocity amplitude for the reference (local) MS configuration. (*B*) The out-of-plane particle-velocity amplitude for the NL-TIR-MS. The comparison of the wave patterns clearly indicates the broadband wave-blocking effect of the NL-TIR-MS compared to a local design.

with a dissipative viscoelastic layer to reduce unwanted reflections, a significant portion of the incident wave was still reflected back into the domain. This behavior is evident in Fig. 10*B* (f = 3,900 Hz), where the first half of the plate in which the source is located gives rise to a typical modal vibration pattern, hence attesting to the finite nature of the domain. Despite these boundary effects, the experimental results show that the underlying waveblocking behavior of the metasurface is still well captured and that the operating frequency range is markedly increased (of approximately a factor of six) compared with the local MS.

Fig. 10 summarizes the results of the experimental measurements in terms of full field data. In particular, Fig. 10 shows the response of both the reference and the NL-TIR-MS waveguides at four selected frequencies ($f_1 = 3.5$, $f_2 = 3.9$, $f_3 = 4.3$, and $f_4 = 4.75$ kHz, marked by the four yellow dashed lines in Fig. 9*D*) within the operating range of the nonlocal metasurface. The response was measured in terms of out-of-plane ($z-$direction) velocity V_z amplitude field. As expected, in the NL-TIR-MS waveguide, the vibrational energy was mostly confined in the area preceding the MS, while only a small fraction propagated through the MS interface. On the other hand, in the reference (local) waveguide, the wave could penetrate the MS practically unaffected. The direct comparison of these wave patterns further support the validity of the intentionally nonlocal concept to achieve passive broadband metasurfaces.

Conclusions

We have presented and experimentally validated the concept of intentional nonlocality in order to design passive elastic metasurfaces capable of broadband performance. Contrarily to the classical (local) metasurface design, where wave control is achieved by engineering the phase gradient via local resonances, in the nonlocal design, the response at a point of the metasurface depends simultaneously on the response of multiple distant points along the interface. This unique behavior was achieved via the use of specifically designed connecting elements that, by coupling together multiple spatially distributed units, resulted in wavenumber-dependent effective elastic properties and carefully tuned effective dynamics of the metasurface. These coupling elements were inspired from the idea of action-at-a-distance, typical of nonlocal microscopic structures, and were designed to implement a macroscopic representation of this concept.

Dedicated modeling tools were also developed in order to account for the nonlocal coupling forces between unit cells and to characterize the dynamic behavior of nonlocal supercells. As a practical example, the methodology was applied to the design of a broadband total internal reflection metasurface. The performance of this design was validated via both full-field numerical simulations and experimental testing. Both results confirmed the validity of the nonlocal concept and the ability to achieve significant broadband performance via a fully passive approach.

While the nonlocal design was tested on a TIR-type metasurface, the concept is very general, and it is expected to be applicable to any kind of metasurface. The ability to overcome the intrinsic narrow-band nature of traditional metasurface designs is expected to eliminate a significant barrier to the use of these passive wave-control devices and to pave the way to a wide range of practical applications.

Supporting Information. Please see *SI Appendix* for methodology details, additional numerical results, and the design's geometric details.

Data Availability. All study data are included in the article and *SI Appendix*.

ACKNOWLEDGMENTS. This work was supported by Sandia National Laboratories Academic Alliance Program Grant 1847039. Sandia National Laboratories is a multimission laboratory managed and operated by National Technology and Engineering Solutions of Sandia, LLC, a wholly owned subsidiary of Honeywell International, Inc., for the US Department of Energy's National Nuclear Security Administration. With main facilities in Albuquerque, NM, and Livermore, CA, Sandia has major R&D responsibilities in national security, energy and environmental technologies, and economic competitiveness. This paper describes objective technical results and analysis. Any subjective views or opinions that might be expressed in the paper do not necessarily represent the views of the US Department of Energy or the United States Government. H.Z., S.P., and F.S. were partially supported by NSF Grant 1761423 and the Defense Advanced Research Project Agency (DARPA) under Grant D19AP00052. We thank Dr. Dylan Casey and Dr. David Saiz for their fundamental contribution on the metal printing process of the nonlocal units.

1. N. Yu *et al.*, Light propagation with phase discontinuities: Generalized laws of reflection and refraction. *Science* **334**, 333–337 (2011).
2. X. Ni, N. K. Emani, A. V. Kildishev, A. Boltasseva, V. M. Shalaev, Broadband light bending with plasmonic nanoantennas. *Science* **335**, 427 (2012).
3. N. K. Grady *et al.*, Terahertz metamaterials for linear polarization conversion and anomalous refraction. *Science* **340**, 1304–1307 (2013).
4. C. Pfeiffer, A. Grbic, Metamaterial Huygens' surfaces: Tailoring wave fronts with reflectionless sheets. *Phys. Rev. Lett.* **110**, 197401 (2013).
5. F. Aieta *et al.*, Aberration-free ultrathin flat lenses and axicons at telecom wavelengths based on plasmonic metasurfaces. *Nano Lett.* **12**, 4932–4936 (2012).
6. M. Kang, T. Feng, H.-T. Wang, J. Li, Wave front engineering from an array of thin aperture antennas. *Opt. Express* **20**, 15882–15890 (2012).

7. S. Sun *et al.*, Gradient-index meta-surfaces as a bridge linking propagating waves and surface waves. *Nat. Mater.* **11**, 426–431 (2012).
8. L. Huang *et al.*, Dispersionless phase discontinuities for controlling light propagation. *Nano Lett.* **12**, 5750–5755 (2012).
9. Y. Li, B. Liang, Z. Gu, X. Zou, J. Cheng, Reflected wavefront manipulation based on ultrathin planar acoustic metasurfaces. *Sci. Rep.* **3**, 2546 (2013).
10. Y. Li *et al.*, Experimental realization of full control of reflected waves with subwavelength acoustic metasurfaces. *Phys. Rev. Appl.* **2**, 064002 (2014).
11. J. Mei, Y. Wu, Controllable transmission and total reflection through an impedance-matched acoustic metasurface. *New J. Phys.* **16**, 123007 (2014).
12. K. Tang *et al.*, Anomalous refraction of airborne sound through ultrathin metasurfaces. *Sci. Rep.* **4**, 6517 (2014).
13. B. Yuan, Y. Cheng, X. Liu, Conversion of sound radiation pattern via gradient acoustic metasurface with space-coiling structure. *Appl. Phys. Express.* **8**, 027301 (2015).
14. J. Zhao, B. Li, Z. Chen, C. W. Qiu, Manipulating acoustic wavefront by inhomogeneous impedance and steerable extraordinary reflection. *Sci. Rep.* **3**, 2537 (2013).
15. J. Zhao, B. Li, Z. N. Chen, C.-W. Qiu, Redirection of sound waves using acoustic metasurface. *Appl. Phys. Lett.* **103**, 151604 (2013).
16. Y. Zhu *et al.*, Dispersionless manipulation of reflected acoustic wavefront by subwavelength corrugated surface. *Sci. Rep.* **5**, 10966 (2015).
17. K. Tang, C. Qiu, J. Lu, K. Manzhu, Z. Liu, Focusing and directional beaming effects of airborne sound through a planar lens with zigzag slits. *J. Appl. Phys.* **117**, 024503 (2015).
18. Y. Li, X. Jiang, B. Liang, J.-C. Cheng, L. Zhang, Metascreen-based acoustic passive phased array. *Phys. Rev. Applied* **4**, 024003 (2015).
19. B. Liu, W. Zhao, Y. Jiang, Apparent negative reflection with the gradient acoustic metasurface by integrating supercell periodicity into the generalized law of reflection. *Sci. Rep.* **6**, 38314 (2016).
20. B. Liu *et al.*, Experimental realization of all-angle negative refraction in acoustic gradient metasurface. *Appl. Phys. Lett.* **111**, 221602 (2017).
21. N. Yu, F. Capasso, Flat optics with designer metasurfaces. *Nat. Mater.* **13**, 139–150 (2014).
22. H. Zhu, F. Semperlotti, Anomalous refraction of acoustic guided waves in solids with geometrically tapered metasurfaces. *Phys. Rev. Lett.* **117**, 034302 (2016).
23. Y. Liu *et al.*, Source illusion devices for flexural lamb waves using elastic metasurfaces. *Phys. Rev. Lett.* **119**, 034301 (2017).
24. S. Li, J. Xu, J. Tang, Tunable modulation of refracted lamb wave front facilitated by adaptive elastic metasurfaces. *Appl. Phys. Lett.* **112**, 021903 (2018).
25. X. Su, Z. Lu, A. N. Norris, Elastic metasurfaces for splitting SV- and P-waves in elastic solids. *J. Appl. Phys.* **123**, 091701 (2018).
26. H. Lee, J. K. Lee, H. M. Seung, Y. Y. Kim, Mass-stiffness substructuring of an elastic metasurface for full transmission beam steering. *J. Mech. Phys. Solids* **112**, 577–593 (2018).
27. Y. Xu, Z. Yang, L. Cao, Deflecting Rayleigh surface acoustic waves by a meta-ridge with a gradient phase shift. *J. Phys. D Appl. Phys.* **51**, 175106 (2018).
28. X. Shen, C.-T. Sun, M. V. Barnhart, G. Huang, Elastic wave manipulation by using a phase-controlling meta-layer. *J. Appl. Phys.* **123**, 091708 (2018).
29. S. Tol, Y. Xia, M. Ruzzene, A. Erturk, Self-bending elastic waves and obstacle circumventing in wireless power transfer. *Appl. Phys. Lett.* **110**, 163505 (2017).
30. H. Zhu, T. F. Walsh, F. Semperlotti, Total-internal-reflection elastic metasurfaces: Design and application to structural vibration isolation. *Appl. Phys. Lett.* **113**, 221903 (2018).
31. H. Zhu, T. F. Walsh, F. Semperlotti, Experimental study of vibration isolation in thin-walled structural assemblies with embedded total-internal-reflection metasurfaces. *J. Sound Vib.* **456**, 162–172 (2019).
32. Y. Chen, X. Li, H. Nassar, G. Hu, G. Huang, A programmable metasurface for real time control of broadband elastic rays. *Smart Mater. Struct.* **27**, 115011 (2018).
33. J. L. Nowinski, On the nonlocal aspects of the propagation of love waves. *Int. J. Eng. Sci.* **22**, 383–392 (1984).
34. J. L. Nowinski, On the nonlocal theory of wave propagation in elastic plates. *J. Appl. Mech.* **51**, 608–613 (1984).
35. A. C. Eringen, Linear theory of nonlocal elasticity and dispersion of plane waves. *Int. J. Eng. Sci.* **10**, 425–435 (1972).
36. D. G. B. Edelen, "Nonlocal field theories" in *Polar and Nonlocal Field Theories*, A. C. Eringen, ed. (Continuum Physics, Academic Press, New York, NY, 1976), vol. 4, pp. 75–204.
37. M. Chen, E. Abdo-Sánchez, A. Epstein, G. V. Eleftheriades, Theory, design, and experimental verification of a reflectionless bianisotropic Huygens' metasurface for wide-angle refraction. *Phys. Rev. B* **97**, 125433 (2018).
38. A. Díaz-Rubio, V. S. Asadchy, A. Elsakka, S. A. Tretyakov, From the generalized reflection law to the realization of perfect anomalous reflectors. *Sci. Adv.* **3**, e1602714 (2017).
39. A. M. H. Wong, G. V. Eleftheriades, Perfect anomalous reflection with a bipartite Huygens' metasurface. *Phys. Rev. X* **8**, 011036 (2018).
40. Y. Ra'di, D. L. Sounas, A. Alù, Metagratings: Beyond the limits of graded metasurfaces for wave front control. *Phys. Rev. Lett.* **119**, 067404 (2017).
41. A. Epstein, G. V. Eleftheriades, Synthesis of passive lossless metasurfaces using auxiliary fields for reflectionless beam splitting and perfect reflection. *Phys. Rev. Lett.* **117**, 256103 (2016).
42. A. Ciattoni, C. Rizza, Nonlocal homogenization theory in metamaterials: Effective electromagnetic spatial dispersion and artificial chirality. *Phys. Rev. B* **91**, 184207 (2015).
43. M. Coppolaro, G. Castaldi, V. Galdi, Aperiodic order induced enhancement of weak nonlocality in multilayered dielectric metamaterials. *Phys. Rev. B* **98**, 195128 (2018).
44. K. Mnasri, A. Khrabustovskyi, C. Stohrer, M. Plum, C. Rockstuhl, Beyond local effective material properties for metamaterials. *Phys. Rev. B* **97**, 075439 (2018).
45. D. Lafarge, N. Nemati, Nonlocal Maxwellian theory of sound propagation in fluid-saturated rigid-framed porous media. *Wave Motion* **50**, 1016–1035 (2013).
46. N. Nemati, D. Lafarge, Check on a nonlocal Maxwellian theory of sound propagation in fluid-saturated rigid-framed porous media. *Wave Motion* **51**, 716–728 (2014).
47. N. Nemati, Y. E. Lee, D. Lafarge, A. Duclos, N. Fang, Nonlocal dynamics of dissipative phononic fluids. *Phys. Rev. B* **95**, 224304 (2017).
48. L. Quan, A. Alù, Passive acoustic metasurface with unitary reflection based on nonlocality. *Phys. Rev. Appl.* **11**, 054077 (2019).
49. P. de Andrés, R. Monreal, F. Flores, Quantum size and nonlocal effects in the electromagnetic properties of small metallic spheres. *Phys. Rev. B* **32**, 7878–7889 (1985).
50. A. Moradi, Quantum nonlocal effects on optical properties of spherical nanoparticles. *Phys. Plasmas* **22**, 022119 (2015).
51. L. Wang, Z. Huang, K. Niu, R. Sun, X. Wu, "Study on the nonlocal surface plasmon resonance properties of au nanotubes" in *2016 Progress in Electromagnetic Research Symposium (PIERS) Proceedings* (IEEE, Piscataway, NJ, 2016), pp. 5096–5100.
52. G. Hu, L. Tang, R. Das, S. Gao, H. Liu, Acoustic metamaterials with coupled local resonators for broadband vibration suppression. *AIP Adv.* **7**, 025211 (2017).
53. G. Hu, L. Tang, R. Das, Internally coupled metamaterial beam for simultaneous vibration suppression and low frequency energy harvesting. *J. Appl. Phys.* **123**, 055107 (2018).
54. G. Hu, J. Xu, L. Tang, C. Lan, R. Das, Tunable metamaterial beam using negative capacitor for local resonators coupling. *J. Intell. Mater. Syst. Struct.* **31**, 389–407 (2020).